Computers and Fluids 213 (2020) 104720

Contents lists available at ScienceDirect

Computers and Fluids

journal homepage: www.elsevier.com/locate/compfluid

Temperature effects on the noise source mechanisms in a realistic subsonic dual-stream jet

Romain Biolchini[a,c], Guillaume Daviller[a,*], Christophe Bailly[b], Guillaume Bodard[c]

[a] CERFACS, 31100 Toulouse, France
[b] LMFA, Ecole Centrale de Lyon, 69134, France
[c] Safran Aircraft Engines, Aerodynamics and Acoustics Department, 77550 Moissy-Cramayel, France

ARTICLE INFO

Article history:
Received 10 February 2020
Revised 24 July 2020
Accepted 14 August 2020
Available online 19 September 2020

Keywords:
Dual-stream jet noise
Large-eddy simulation
Temperature effects

ABSTRACT

A detailed numerical investigation of temperature effects on both aerodynamics and acoustics of a dual-stream jet including a central plug is carried out. The geometry is representative of a realistic turbofan with a high by-pass-ratio (BPR) close to 9. Two take-off high-subsonic operating points are investigated numerically by compressible large-eddy simulation. For these two selected points, the secondary stream is exactly the same in terms of static temperature and velocity. Both jets have also the same primary velocity. The only difference lies in the static temperature of the primary jet. There is a ratio of two between the two jets considered in this study, namely $T_j = 400$ K and $T_j = 800$ K. More precisely, the primary jet temperature is reduced while keeping the acoustic Mach number constant, leading to an increase of the primary jet Mach number from $M_j = 0.65$ in the heated case to $M_j = 0.89$ in the cold case. Some experimental data are available for the hot jet while the cold jet is introduced for academic reasons. The heated jet compares reasonably well with the experimental data, taking into account the complexity of the geometry. Temperature effects have a limited impact on aerodynamic development and acoustic radiation. The influence of the core flow is found to be weak due to the high BPR considered and the radiated acoustic is mainly driven by the secondary flow. Further investigations are carried out in order to highlight the differences between the two cases. The acoustic production area are identified by the way of axial velocity skewness coefficient maps. Finally, a decrease of the primary stream temperature leads to the development of trapped acoustic waves inside the jet core. An increase of the overall sound spectrum level about 5 dB is thus observed in the upstream direction for the cold jet, in agreement with the vortex sheet theory.

1. Introduction

Noise pollution produced by commercial aircraft is a major environmental challenge in the next few years. Despite the mechanical reduction of noise induced by the architecture evolution of turbofan engines, with the increase of the fan diameter and the by-pass ratio, the propulsive jet remains a major component to the total noise during the take-off phase. As a consequence, research efforts on jet mixing noise are being pursued through experimental investigations and numerical studies. The latter have a privileged role, in particular compressible large-eddy simulation (LES), to directly obtain the turbulent flow and the radiated acoustic field in a large physical domain [1–4]. An increasingly clear picture of the role played by different turbulent flow regions for acoustic radiation has emerged over time, at least for isolated subsonic jets. The importance of initial conditions for convective shear flows has also been pointed out [5], in connection with the value of the Reynolds number in numerical simulations.

The noise radiated by dual-stream jets has also been investigated. Numerically, a direct noise computation of a coplanar coaxial hot jet has been performed by Bogey et al. [6]. Increasing the complexity of the geometries, Viswanathan et al. [7] have studied the flow field and noise from dual beveled nozzles. The influence of numerical parameters on the noise radiated by a dual-stream jets of a short cowl nozzle has been investigated by Andersson et al. [8] using a block-structured finite-volume approach. Unstructured meshes [9] are, however, most often used to tackle such complex configurations. The numerical simulation of convective coaxial turbulent flows with the presence of multiple velocity and temperature gradients, requires the use of high-order numeri-

* Corresponding author.
E-mail address: guillaume.daviller@cerfacs.fr (G. Daviller).

https://doi.org/10.1016/j.compfluid.2020.104720
0045-7930/

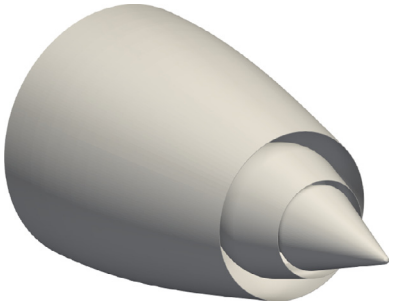

Fig. 1. Geometry of the baseline EXEJET nozzle [16].

cal solvers and suitable turbulence models [10,11]. A good overview of best practices for jet aeroacoustics can be found in the work by Brès et al. [12], see also references herein.

Only a few experimental [13,14] studies deal with more realistic configurations. The EXEJET experimental project [15] was conducted in order to document the noise radiated by a realistic jet having a bypass ratio of 9, including flight effects, the presence of a plug nozzle and also possible installation effects. The baseline nozzle geometry is shown in Fig. 1. The turbulent flow and noise database [16] is representative of new airliners operating at take-off conditions, and was generated to support the validation of advanced numerical tools. In the present study, one operating point selected from the EXEJET database is simulated, corresponding to a take-off condition without flight effects. The primary stream is characterized by a high speed subsonic stream and a static temperature $T_j = 800$ K. In addition, a second point, not present in the database, is also computed with the same nominal parameters except the static temperature of the primary stream, $T_j = 400$ K. The aim of the present work is to complement the EXEJET experimental project with a numerical investigation based on LES. The objective is to have a thorough knowledge of the flow and noise radiated by coaxial jets exhausting from a plug nozzle, with a focus on temperature effects induced by the primary hot stream.

Temperature effects on jet noise still remain a tricky problem in aeroacoustics, even for an isolated single jet. Pioneering experimental studies [17,18] have shown the emergence of an additional noise component related to entropy fluctuations, as predicted by Lighthill's analogy [19]. There is however no general agreement regarding extra sources associated with entropy fluctuations. Indeed, related measurements have recently been completed by Viswanathan [20] and Bridges & Wernet [21], by avoiding two pitfalls. First, the heating system itself can introduce a spurious noise component in such experiments. Second, increasing the temperature for a given geometry decreases the Reynolds number value of the jet. As observed experimentally by Zaman [22] and numerically by Bogey et al. [23], a too low Reynolds number value ($Re_j < 10^5$) will not allow a turbulent state of the boundary layer at the nozzle exit. These difficulties can be partly overcomed by numerical simulations, and the reader can refer to the study by Bogey & Marsden [24] for a deeper discussion regarding the separation of temperature effects with respect to Reynolds number effects. Furthermore, Towne et al. [25] have shown that an acoustic resonance could appear in the potential core for particular velocity and temperature exhaust conditions, whose characteristics can be predicted by a vortex-sheet model.

Fisher et al. [26] have developed a semi-empirical model based on dimensional laws for a coaxial jet. The radiated noise is basically obtained by the quadripolar contribution of the cold secondary flow and the dipolar contribution of the hot primary stream, that is noise induced by velocity fluctuations and temperature fluctuations respectively. More recently, Viswanathan [27] has performed a parametric study on temperature effects in dual-stream jets. For fixed Nozzle Pressure Ratio in both primary (NPR=2.1) and secondary (NPR=1.6) jets, the author has observed that the increase of primary jet's temperature leads to a uniform increase of sound pressure level (SPL) for all angles of observation. A cold subsonic secondary stream at fixed Mach number $M = 0.85$ and a slightly supersonic primary stream with different exit velocities (depending on the temperature ratio) were considered. As a consequence, it is difficult to link the increase of the SPL to the temperature ratio of the primary jet only.

In the present work, two large-eddy simulations based on the realistic turbofan jet nozzle, displayed in Fig. 1, are performed in order to investigate the noise radiated by a dual-stream jet in the presence of temperature effects. The two operating points and the nozzle design are first described. The numerical methodology, the mesh construction and the inflow boundary conditions are provided in a next section. The aerodynamic behaviour of both jets is then analyzed and compared to available experimental data, with a specific investigation on temperature fluctuations. The acoustic far field is extrapolated from a control surface and the radiated sound field is studied in a subsequent section. Numerical predictions are again validated with available measurements. The last section is devoted to the identification of a strong acoustic resonance taking place in the primary stream, leading to acoustic tones observed in the far field [28,29]. The model developed by Towne et al. [25] is applied with success to predict this behaviour as a function of the temperature ratio between the two streams. Concluding remarks are finally drawn.

2. Geometry and flow parameters

The dual-stream nozzle considered in this study includes a central plug, as shown in Fig. 1, and corresponds to the baseline configuration in Huber et al. [15] for a nominal bypass ratio of 9. In order to investigate temperature effects, two subsonic operating points at take-off conditions without flight effects have been retained. The first dual-stream jet, denoted T800, has a hot primary stream and corresponds to a point documented in the database [15]. The second, denoted T400, has been defined for academic purposes with a cold primary stream, but has no experimental counterpart. The primary exhaust velocity of both jets are the same, and only the temperature of the primary stream differs. However, whereas the acoustic Mach number is keep constant for the two case, a temperature decrease at constant exhaust velocity leads to an increase of the jet Mach number. The jet properties of the secondary stream are identical. To validate the LES simulation of the jet T800, the following measurements extracted from the EXEJET database can be used: first, the mean flow field from Particles Image Velocimetry (PIV) data without flight effects; second, five-hole probe measurements coupled with thermocouples at the nozzle exhaust with flight effects; and third, sound pressure levels in the far field at $r = 40D^s_{\text{ef}}$ for polar angle between 30° and 140°, again without flight effect. For the second set of measurements, it is assumed that the primary and secondary streams at the nozzle exit are not affected by flight effects.The effective diameter of the secondary stream D^s_{ef} is defined as the difference between the secondary stream diameter and the primary stream nacelle diameter at the secondary jet exit plane, that is $D^s_{ef} = \sqrt{D^{s2}_j - D^2_p(x = x^s_{ep})}$, where x^p_{ep} and x^s_{ep} are the axial coordinate of the primary and secondary flow exhaust planes. The primary effective aerodynamic diameter is defined as $D^p_{ef} = \sqrt{D^{p2}_j - D^2_{plug}(x = x^p_{ep})}$. The notations are also displayed in Fig. 2 (b), along with the computational domain at the nozzle exhaust. Details about acoustic measurements can be found in [15], whereas methodologies about PIV and five-hole probe measurements are presented in David et al. [16].

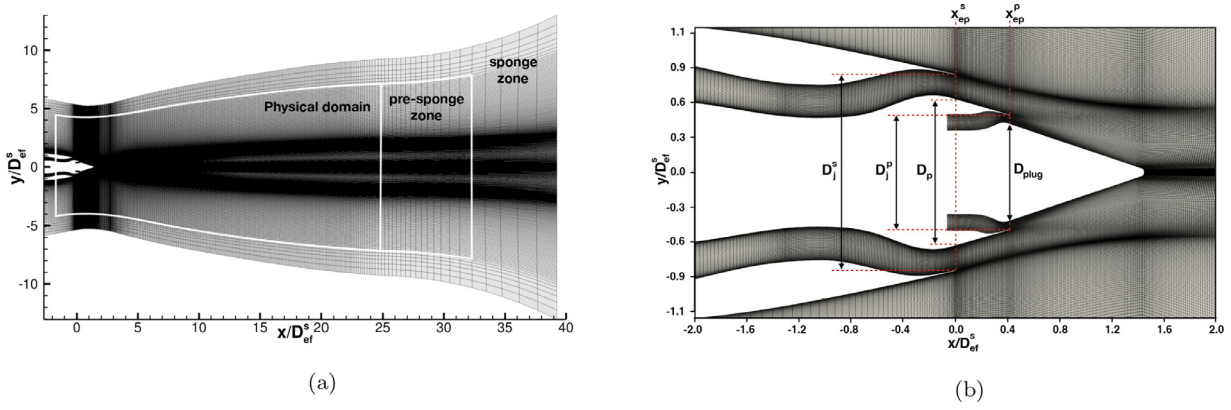

Fig. 2. Mesh of the computational domain containing the jet axis, only every second point is shown: (a) whole computational domain (b) zoom around the nozzle exit.

Table 1
Flow properties of the two jets T800 & T400 [15].

	primary stream				secondary stream			
jet	M^p	M^p_j	T^p_j (K)	Re^p_D	M^s	M^s_j	T^s_j (K)	Re^s_D
T800	1.07	0.65	776	5.5×10^5	0.84	0.82	286	3.8×10^6
T400	1.07	0.89	405	1.7×10^6	0.84	0.82	286	3.8×10^6

The flow properties of both jets are summarized in Table 1. Both jet flows are characterized by an acoustic Mach number of $M^p = U^p_j/c_0 = 1.07$ for the primary stream and $M^s = U^s_j/c_0 = 0.84$ for the secondary stream, where U_j denotes the primary exhaust velocity and c_0 the ambient speed of sound. The superscripts .^{p}, and .^{s} are respectively associated with the primary and secondary streams. In addition, M_j stands for the Mach number of the jet and T_j for the exhaust static temperature.

The T800 case is characterized by a temperature ratio of $T^p_j/T^s_j = 2.7$ and a diameter-based Reynolds number of the primary jet $Re^p = U^p_j D^p/\nu_j = 5.5 \times 10^5$. In the T400 case the temperature ratio is 1.4 and the Reynolds number is $Re^p = 1.7 \times 10^6$. The Reynolds number of the secondary stream is $Re^s = U^s_j D^s/\nu_j = 3.8 \times 10^6$ for both cases. The two jet parameters have been chosen to preserve a primary stream Reynolds number value for the hot case greater than the threshold around 4×10^5, for which Reynolds number effects can interfere with temperature effects [20].

3. Numerical methods

3.1. Flow solver

The present numerical simulations have been performed with the *elsA* solver [30]. The compressible Navier-Stokes equations are solved on structured body-fitted grids using a finite volume formulation. Optimized finite-difference schemes developed for computational aeroacoustics are implemented. The temporal discretization is performed by a six-step Runge-Kutta scheme, developed by Bogey et al. [31]. In the two simulations, the same time step Δt is chosen to satisfy the Courant-Friedrichs-Lewy criterion CFL = 0.9 for both jets. A sixth-order compact scheme adapted by Fosso et al. [32] is used for the spatial discretization, combined with a sixth order compact filter proposed by Visbal & Gaitonde [33]. This filter also acts as an explicit subgrid scale model. As a consequence, small scales discretized by less than four points perwavelength are removed without affecting the larger scales of the turbulent flow [34].

The boundary conditions used for the Reynolds-averaged Navier-Stokes (RANS) simulations are imposed as follows. At the inlet of each duct, an in-going subsonic condition prescribes the total pressure P_t, the total temperature T_t is then used to get the target Mach number (see 1). The ambient pressure is imposed on the side and downstream limits. To ensure stability and a faster convergence of the simulations, a low co-flow ($u/U^p_j = .05$) is imposed on the free stream inflow around the nozzle. Finally adiabatic no-slip wall conditions are applied to the nozzle surface. In LES, a three dimensional formulation of acoustic radiation conditions [35] based on Tam and Dong conditions [36] is imposed on the side and downstream boundaries of the computational domain. Moreover, a sponge zone is added when the convective flow leaves the physical domain. In this zone, the grid is stretched by a ratio of 10% in order to dissipate the most energetic turbulent structures. This numerical procedure is however not sufficient, and some spurious waves can still be generated. A second-order filter combined with a cooling term [37] are also applied in the sponge zone. This outflow condition has shown the best results in the ***elsA*** software [38]. The inflow conditions of both streams are prescribed using the radiative boundary condition of Tam and Webb [39]. As for outflow boundary conditions, a sponge zone where a cooling term is applied to the conservative field to preserve exhaust conditions is used in the LES stages [40]. The turbulent state of the incoming flow is mimicked by the addition of a vortex ring tripping. The aim of such procedure is not to reach a fully developed turbulent boundary layer, which is overly demanding in CPU cost, but to mimic this stage. All the detail of the procedure is explain in Bogey et al. [41]. The vortex center is added in the nozzle boundary layer, at $r_{vr} = r_{wall}(x_{vr}) - \delta_0(x_{vr})$ where r_{vr} and x_{vr} are respectively the radius and the axial coordinate of the vortex ring center, $r_{wall}(x_{vr})$ the radius of the wall at x_{vr} and $\delta_0(x_{vr})$ the boundary layer thickness at x_{vr}. In the primary stream $x_{vr} = -0.018D^s_j$ and $\delta_0(x_{vr}) = 0.003D^s_j$, while in the secondary flow $x_{vr} = -0.9D^s_j$ and $\delta_0(x_{vr}) = 0.017D^s_j$. In the LES, a wall law based on Reichardt's analytical expression [42] is applied to all the walls. More details on the implementation of this numerical procedure in a high-order workflow can be found in Le Bras et al. [11].

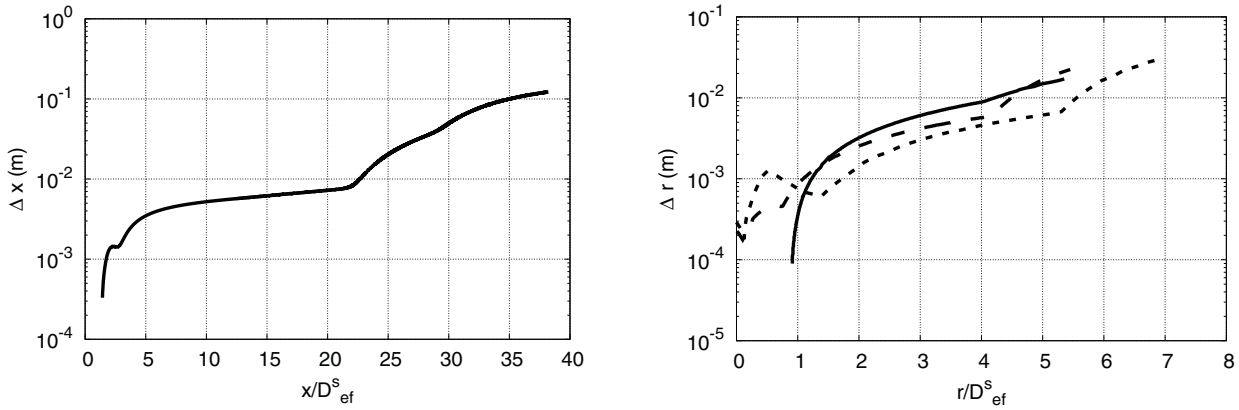

(a) (b)

Fig. 3. Mesh distribution along: (a) the centerline and (b) radial lines at $x = 0.65D^s_{ef}$ (——), $3.3D^s_{ef}$ (– – –) and $10D^s_{ef}$ (……).

3.2. Mesh construction

A view of the computational domain is shown in Fig. 2 (a). The total length of the domain is approximately $39D^s_{ef}$ in the axial direction and $11D^s_{ef}$ in the radial direction at $x = 0$. The dimensions of the physical domain are approximately $25D^s_{ef}$ in the axial direction and $8D^s_{ef}$ in the radial direction at $x = 0$. The origin of the coordinate system is placed on the jet axis and in the secondary stream exit plane. The outer shape of the computational domain follows the jet flow expansion in the physical domain and the mesh stretching in the sponge zone as explained below.

The mesh is constructed with the aim to ensure a cut off frequency f_c of 7500 Hz for acoustic waves in the physical domain on the largest grid cell, which corresponds to the Strouhal cut-off number $\mathrm{St} = f \times D^s_{ef}/U^s_j = 4$. The second limit is the mesh size at the wall, which is constructed to obtain a distance in wall unit of $y^+ = yu_\tau/\nu = 40$ with u_τ the friction velocity. The expansion ratio is maintained under 4% in the physical domain to avoid the production of spurious noise. In the nozzle, the grid size in the axial direction is constant and chosen as $\Delta x = 3\Delta r_{wall}$ to ensure a good discretization of turbulence. The total mesh size is about 256×10^6 cells with $N_x = 1200$, $N_r = 600$ and an azimuthal discretization $N_\theta = 256$. This leads to an azimuthal grid size of $\Delta\theta^p = 8\Delta r_{wall}$ and $\Delta\theta^s = 15\Delta r_{wall}$ on the primary jet leap and on the secondary jet leap, respectively. The grid spacing at the secondary nozzle exhaust in the axial and azimuthal direction in wall unit are $x^+ = 180$ and $\theta^+ = 680$, respectively. The same mesh is used for the two operating points.

In Fig. 2 (b) refinement zones are also clearly visible close to the nozzle exit planes and in the shear layers. The mesh distribution on the centerline and on radial lines for three axial positions $0.65D^s_{ef}$, $3.3D^s_{ef}$ and $10D^s_{ef}$ are plotted in Fig. 3 (a) and (b) respectively. As shown in Fig. 3 (a), the smallest axial discretization is located just after the plug tip with $\Delta_x = 3 \times 10^{-4}$ m. Then, the mesh is stretched in the axial direction until $x = 5D^s_{ef}$, which corresponds to the merging point of the two streams. After this position, the axial distribution increases to reach the maximal mesh size $\Delta_x = 8 \times 10^{-3}$ m at $x = 22D^s_{ef}$. In the axial direction, a pre-sponge layer is added before the sponge zone in order to obtain a smoother transition between the physical zone and the sponge zone.

3.3. Simulation stages

In order to prescribe the initial conditions at the boundaries with accuracy, a two stage RANS-LES calculation is applied. This methodology has been developed by Shur et al. [43–45]. First, the boundary conditions are computed by a RANS simulation with a Spalart-Allmaras turbulence model [46]. For this kind of simulation a dedicated RANS mesh is used, which is wall-resolved in the entire nozzle to obtain an accurate description of the boundary layers. This mesh is composed by a total of 13×10^6 cells. The computation reaches a converged state when the residuals are reduced by three orders of magnitude using the Roe third-order spatial scheme.

The RANS solutions at the secondary stream exit $x = 0$ are compared with the five-hole probe from T800 experiment (with flight effects, see Section 2) in Fig. 4, for the radial profile of the mean axial velocity (a) and the temperature (b). Keeping in mind that the conditions for T800 and T400 are identical for the secondary stream, consistent results are obtained and compare well with experiment [15]. The differences observed for $y > 0.5D^s_j$ are due to the flight effect in the experiment, not taken into account in the simulations. As a consequence, a boundary layer is present on the external part of the nacelle in the experiment. The non-zero flow around the nacelle is induced by the small coflow added in the simulation, see Section 3.1, and also by entrainment.

Fig. 5 (a) and (b) show respectively the axial velocity and temperature radial profiles at the primary stream exit $x = 0.25D^s_j$. Velocity profiles of the primary stream are identical for both cases (as defined in Table 1) and are in agreement with experimental data ($y < 0.3D^s_j$). Regarding the differences on the velocity profile for $y > 0.3D^s_j$, they are again due to the flight effect which is not take into account here. The radial temperature profile in the primary jet is also in agreement with experiment for the case T800 and divided by two for the case T400.

In Figs. 4 and 5, the radial profiles obtained by LES at the same localization are also plotted. It can be observed that the inflow boundary conditions used in both LES allow to retrieve the exhaust velocity profiles of both streams.

An additional step is performed between the RANS simulation and the high-order LES. It consists of the computation of a transitional flow with Roe third-order scheme on a coarser grid. This coarse grid has only one point over two in each direction which divides by eight the total number of cells compare to the full mesh. Including the transient time needed to obtain an instantaneous solution from a stationary one, this procedure led to a saving of 30% of CPU time during the transition step between a classical computation and the LES low-order methodology. The last step of the process is finally to compute the flow with the high-order algorithm and on the full resolved mesh. The low order solution is first

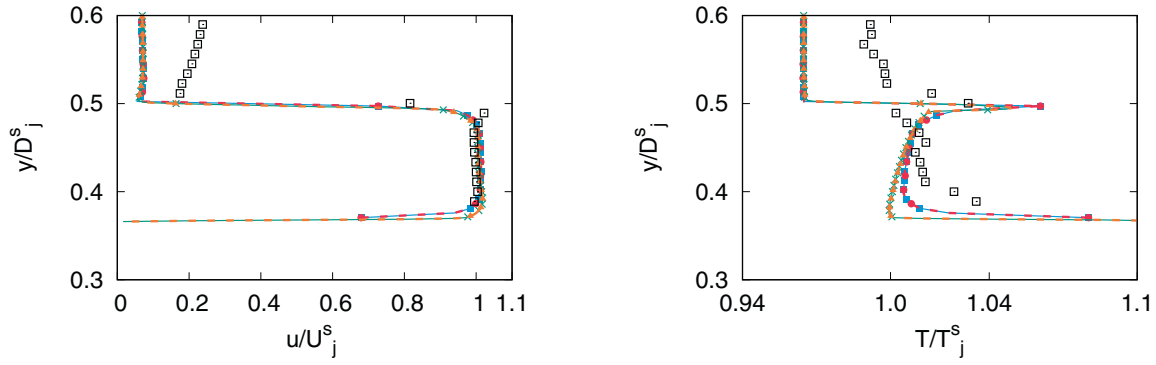

(a) (b)

Fig. 4. Radial profile at the nozzle exit of the secondary flow $x = 0$: (a) axial velocity and (b) static temperature. RANS : —●— T800 ; —■— T400; LES : —▲— T800; —×— T400 and ⊡ Experiment [16].

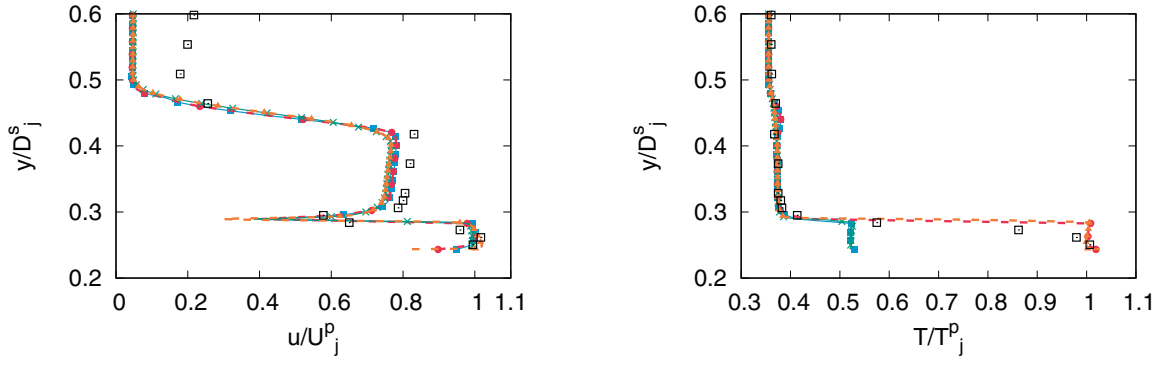

(a) (b)

Fig. 5. Radial profile at the nozzle exit of the primary flow $x = 0.25D^s_j$: (a) axial velocity and (b) static temperature. RANS : —●— T800 ; —■— T400; LES : —▲— T800; —×— T400 and ⊡ Experiment [16].

Table 2
Simulation times of the three step for both cases T800 & T400.

	Iterations	$\Delta t(s)$	$T(ms)$	$T \times U^p_j/D^p_j$	$f_{\min}$ (Hz)	$\mathrm{St}_{\min}$	CPU time / simulation (kh)
(1) RANS	310×10^3	-	-	-	-	-	4
(2) LES	300×10^3	1×10^{-7}	30	90	-	-	35
(3) LES	950×10^3	3×10^{-8}	30	90	350	0.2	1 160

evacuated from the computational domain before starting the flow statistics record. During this stage, the time step is $\Delta t = 3 \times 10^{-8}$s and the total simulated time is $T = 32.5$ms. Assuming that a temporal event is resolved if the total time contains 10 times its periods, the minimal frequency associated with the simulation time is $f_{\min} = 350$Hz or $\mathrm{St}_{\min} = f \times D^s_{ef}/U^s_j = 0.2$. All computation times are summarized in Table 2.

4. Analysis of aerodynamic fields

An instantaneous snapshot of the T800 jet flow field in the physical LES domain, identified from the vorticity norm $|\Omega| = \sqrt{\omega_x^2 + \omega_y^2 + \omega_z^2}$ is shown in Fig 6. The acoustic radiation is also depicted with a map of the fluctuating pressure. The vorticity field exhibits large structures after $x = 5D^s_{\mathrm{ef}}$ and smaller one close to the nozzle exit and the central plug. No spurious wave is identifiable in the acoustic field. The jet noise directivity is characterized with low frequency waves traveling downstream and higher frequency waves propagating perpendicular to the nozzle. Differences are too

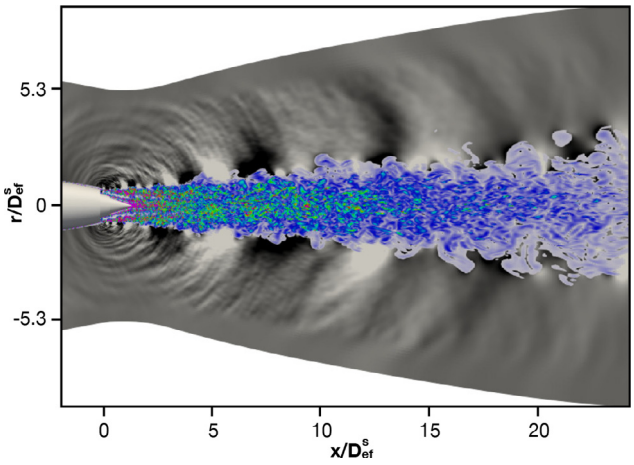

Fig. 6. T800 case: Instantaneous vorticity field $4 \times 10^2 \leq |\Omega|(s^{-1}) \leq 3 \times 10^6$ superimposed on the fluctuating pressure field $-200 \leq p'(\mathrm{Pa}) \leq 200$ in the physical domain of the simulation.

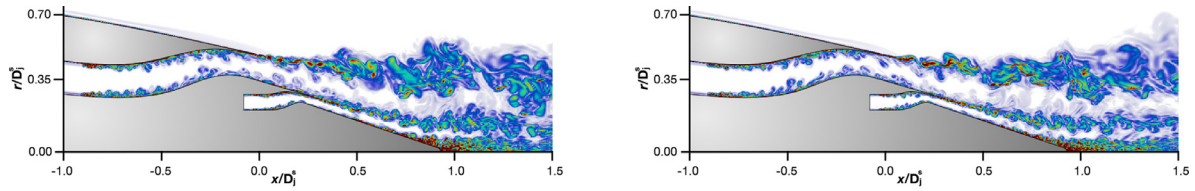

(a) T800 (b) T400

Fig. 7. Longitudinal plane of the instantaneous vorticity modulus $5 \times 10^2 \leq |\Omega|(s^{-1}) \leq 3 \times 10^6$ in the vicinity of the nozzle exit.

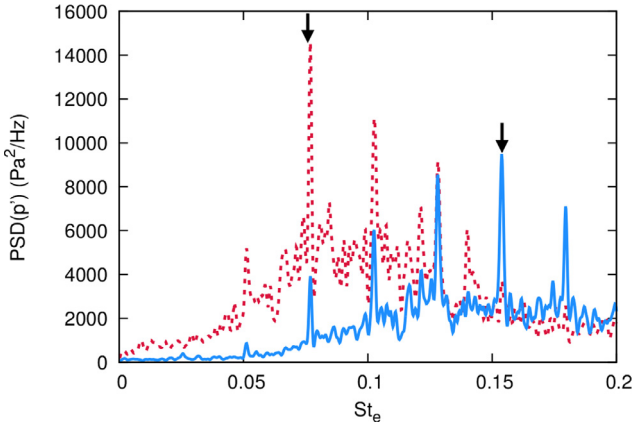

Fig. 8. T800 case: PSD of pressure fluctuations at $r = 0.44D_j^s$ for axial positions : —— $x = 0.2D_j^s$ and - - - $x = 0.3D_j^s$. Arrows mark the frequencies $St_0 = 0.154$ and $St_0/2 = 0.076$.

minor to perform a visual comparison with the T400 jet, which has the same secondary stream.

4.1. Vorticity field in the vicinity of the nozzle exit

A longitudinal plane of the vorticity modulus close to the nozzle exit is presented in Fig 7 for both jets T400 (a) and T800 (b). The jet flow development looks very similar and no significant difference appears due to temperature effects. Turbulence in both boundary layers and the jet flow seem to be fully developed. Small and large turbulent structures can be seen as expected in flow with such high Reynolds number. The turbulent activity in the area downstream the plug tip is high. The boundary layer tripping is applied at $x = -0.9D_j^s$ in the secondary stream and at $x = 0$ for the primary stream. Resulting perturbations are thus convected by the mean flow up to the nozzle exit. Nevertheless, a vortex shedding phenomenon occur downstream the nozzle lip of the secondary stream. This phenomenon is difficult to identify for high Reynolds number flow and has a real impact on radiated noise as shown by Bogey [47].

In order to characterize the vortex shedding, pressure spectra are computed along the secondary flow shear layer ($r = 0.44D_j^s$) in the T800 case. The power spectral density (PSD) of the pressure for axial positions $x = 0.2D_j^s$ and $0.3D_j^s$ are plotted in Fig. 8. The Strouhal number $St_e = f \times e/U_j^s$ is based on the secondary nozzle lip thickness e and the secondary stream exhaust velocity U_j^s. At $x = 0.2D_j^s$ (solid line), the PSD is dominated by a peak frequency at $St_0 = 0.154$. This frequency peak is the fundamental frequency St_0 of the von Kármán vortex street based on the secondary nozzle lip thickness e. In the same spectrum, subharmonic frequencies are also visible due to non-linearity effects [6]. Downstream, at $x = 0.3D_j^s$ (dashed line), the subharmonic peak at $St_e = 0.076$ is predominant. This frequency is close to $St_0/2$, and is directly associated with vortex pairings occurring in the external shear layer. This event can be also seen in Fig. 7 Despite the inner boundary layer tripping, the limited azimuthal discretization leads to highly anisotropic cells at the secondary stream exit, and avoid the development of a fully turbulent flow. The same result is observed in the T400 jet.

4.2. Comparisons of the velocity field with PIV for the T800 case

Comparisons are performed in Fig. 9 for the mean axial velocity radial profile from PIV planes at $x = 2D_{ef}^s$, $10D_{ef}^s$, and $14D_{ef}^s$. For each position, the jet growth rate is slightly overestimated. Nevertheless, at $x = 2D_{ef}^s$, the thickness of the primary stream is in agreement with experiment whereas only the secondary stream thickness is overestimated. Moreover the axial velocity amplitude for the secondary stream is slightly underestimated compared to the PIV measurements. This difference tends to disappear for downstream positions.

Overall, comparisons between LES and experiment for the mean axial velocity are in good agreement. These differences could be explained by different factors but mostly due to the mesh discretization. Indeed, as mentioned before, the large mesh size in the azimuthal direction leads to a vortex pairing phenomenon. This means that too strong coherent vortices exist downstream the nozzle exit of the secondary stream in the shear layer, regarding this high Reynolds number flow type. As observed previously by Bodony [48], organized turbulent structures could lead to an increased rate of the velocity decay induced by approximations in the LES modeling.

4.3. Jet flow aerodynamic downstream the nozzle

In Fig. 7, the jet flow is fully attached to the nozzle wall for both cases. This observation based on instantaneous vorticity modulus field is confirmed with streamlines of the mean velocity field shown in Fig. 10. In particular, the boundary layer on the central plug remains also fully attached. The numerical ingredients (wall law, tripping) used in these simulations, combined with the mesh discretization, allows to obtain a realistic flow field with a turbulent boundary layer and no flow separation, as expected and observed in experiments in such configurations [49]. On the contrary, as underlined by Brès et al. [50], laminar nozzle boundary layers could lead to an unrealistic flow separation and spurious noise prediction.

Fig. 11 shows the radial profiles of the mean axial velocity, which look very similar for both cases. Indeed, as the exhaust velocity of the primary jet is kept constant in the two simulations, temperature effects on the aerodynamics for this non-potential jet flow are limited. Moreover, the velocity defect in the plug wake is weak and disappears rapidly. Indeed, at $x = 1D_j^s$ the velocity defect is about 35% whereas at $x = 2D_j^s$ it is about 4%. However, some differences are observed on the radial profiles of the axial velocity fluctuations plotted in Fig. 12. In particular, the intensity of the turbulence is higher in the shear layer for the T800 case in the

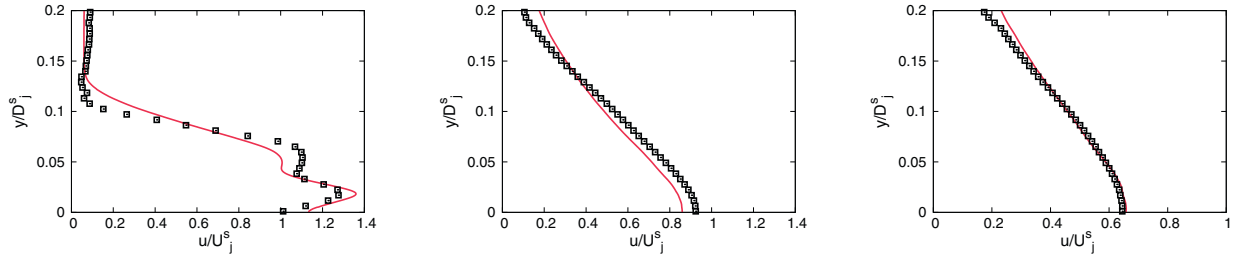

Fig. 9. T800 case: mean axial velocity along a radial profile at : (a) $x = 2D^s_{ef}$, (b) $x = 10D^s_{ef}$ and (c) $x = 14D^s_{ef}$. — LES and ⊡ Experiment [16].

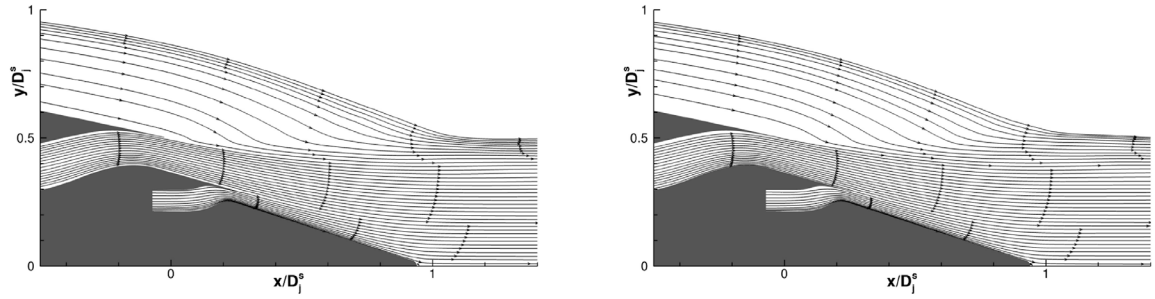

Fig. 10. Streamlines in the vicinity of the dual-stream nozzle.

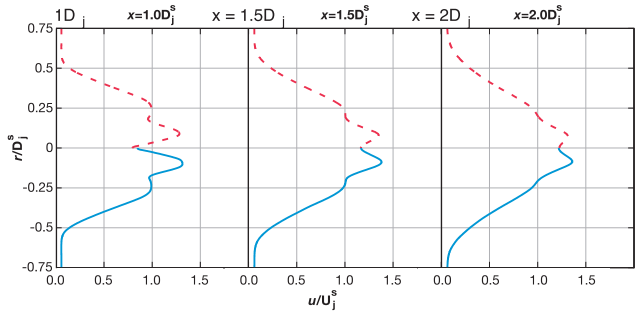

Fig. 11. Mean axial velocity profile in the plug wake. — — T800; — T400.

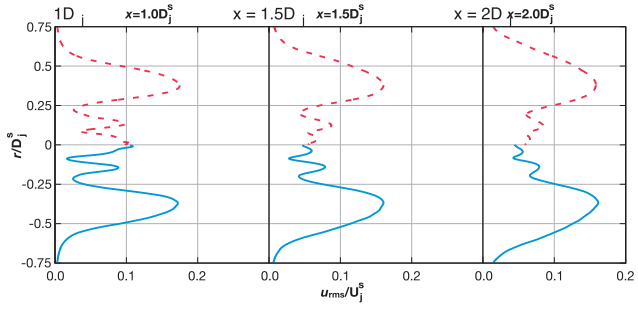

Fig. 12. Axial velocity fluctuations profile in the plug wake. — — T800 (top); — T400 (bottom).

primary stream, i.e. for $-0.2 \leq r/D^s_j \leq 0.2$. That suggests that the turbulent coherent structures contain more energy due to temperature increase. The same behavior is observable in a hot single stream jet as shown in numerical [51] and experimental studies [52].

For an axial spacing ξ and a temporal separation τ, the two-point space-time correlation of the fluctuating axial velocity u' is

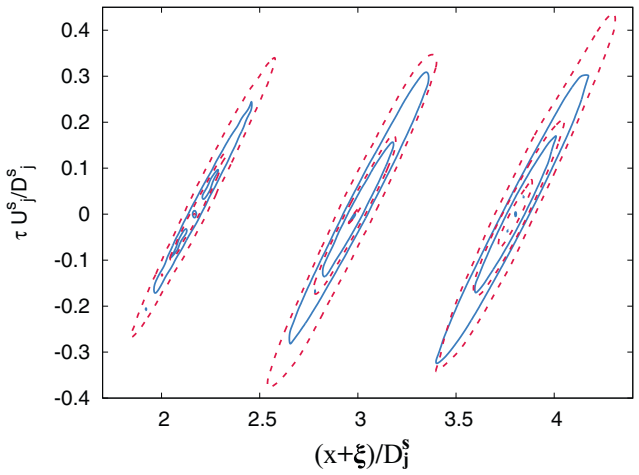

Fig. 13. Two-point space-time correlations of the axial velocity along the jet axis $R_{uu} \in [0.5, 0.75, 1.0]$ for $x = 2.16D^s_j$, $x = 2.96D^s_j$ and $x = 3.80D^s_j$. — — T800; — T400.

defined as

$$R_{uu}(x, \xi, \tau) = \frac{\langle u'(x,t)u'(x+\xi, t+\tau)\rangle}{\sqrt{\langle u'^2(x)\rangle}\sqrt{\langle u'^2(x+\xi)\rangle}}, \tag{1}$$

where x and t are the spatial position on the jet axis and the time where the two-point correlation is evaluated, respectively. Two-points space-time correlations based on axial fluctuating velocity on the jet centerline are plotted in Fig. 13. The spatial separation is $\Delta\xi = 4 \times 10^{-2} D^s_j$ and the time step is $\Delta\tau = 1.8 \times 10^{-2} U^s_j D^s_j$.

From Fig. 13, it can be observed that turbulent scales are larger in space and longer in time for the T800 case and for axial positions $x/D^s_j \leq 4$, which confirms observations made from Fig. 12. In the simulation of T800 case, an increase of temperature leads to an increase of turbulence coherence. These observations were also

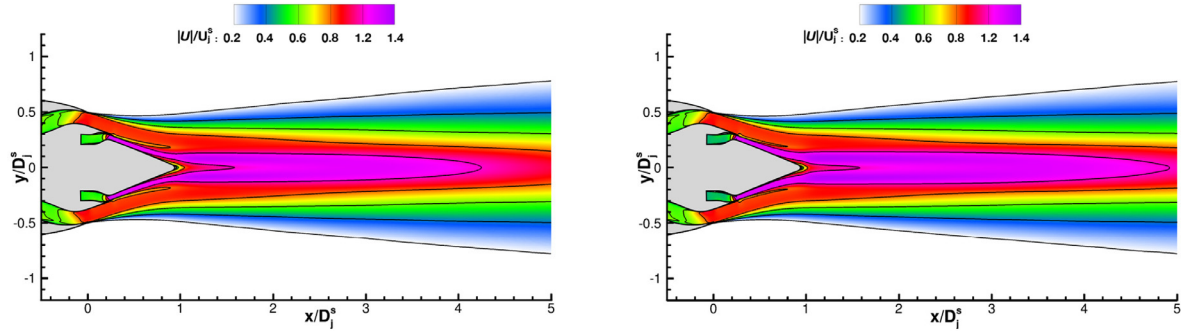

(a) T800 (b) T400

Fig. 14. Longitudinal axial plane of the mean axial velocity for (a) T800 and (b) T400.

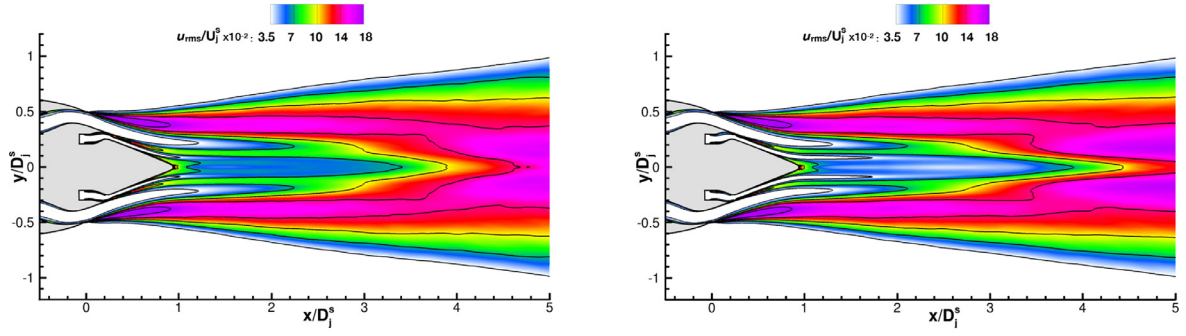

(a) T800 (b) T400

Fig. 15. Longitudinal axial plane of the axial velocity fluctuations for (a) T800 and (b) T400.

done by Bridges [53] on a hot single stream jet. However, temperature effects do not modify the convection velocity on the jet axis.

4.4. Temperature effects on the mean axial velocity and turbulence

In order to investigate temperature effects, the mean axial velocity map of the two configurations T800 and T400 are respectively presented in Fig. 14 (a) and (b). The plug does not allow the development of a classical potential flow, as encountered for a single jet. A jet core length can still be defined such as $u(x_c) = 0.95 \times \max(u(r=0))$ where x_c is the jet core length. Following this definition, the jet core length is $x_c = 4D_j^s$ for the case T800 and $x_c = 4.54D_j^s$ for the case T400.

As for a single jet [54], a temperature increase leads to a shorter jet core length caused by an increase of the turbulent intensity in the primary stream, as shown in Fig. 12 and Fig. 15. Except this difference, the two flows are quite similar regarding the mean axial velocity. Same conclusions can be drawn regarding the fluctuating velocity in Fig. 15. This result can be explained by the high by-pass ratio of the present dual-stream geometry. Temperature effects on the global mean flow and turbulence are restricted to the primary stream and no significant differences are noticed after the mixing of the two stream for $x/D_j^s \geq 5$.

4.5. Skewness of velocity and temperature

Bogey [51] has shown that a negative skewness of aerodynamic values, such as the axial velocity, is a good indicator of low frequency acoustic production in a single free jet. The location of the skewness peak is consistent with the correlation peak between velocity fluctuations on the central axis and the acoustic pressure in the near field. In order to identify a possible region of acoustic production in this dual-stream jet, a two dimensional mapping of the axial velocity skewness $u_{skew} = \overline{u'u'u'}/\overline{u'u'}^{3/2}$ is plotted in Fig. 16 (a) for the T800 jet and (b) for the T400. The skewness fields are plotted for $r \leqslant 0.2D_j^s$, that is in the region where intermittency is expected to be significant. Two zones can be distinguished, the growing shear layers associated with entrainment and mixing, and the coalescence of these shear layers at the end of the potential cone. Isolines of the axial velocity standard deviation are also superimposed to facilitate interpretation.

In both cases, the maximum amplitude of the skewness factor is approximately $u_{\text{skew}} = -2$ and observed around the end of the jet core. In addition, for the case T400, this maximum is also located in the shear layer in the transition region before the end of the jet core. This result indicates that the mixing between the two streams in the T400 case leads to more intermittent events and could be responsible for the low frequency acoustic radiation.

5. Acoustic fields

The acoustic radiation is calculated from the integral formulation of the Ffowcs-Williams and Hawkings (FWH) analogy [55]. The input surface for the FWH processing is positioned around the jet aerodynamic structures, represented by vorticity modulus isosurfaces in Fig. 17 The surface starts at $x_i = -2D_{\text{ef}}^s$ with a radius $r(x_i) = 1.3D_{\text{ef}}^s$ and finishes at $x_f = 30D_{\text{ef}}^s$ with a radius $r(x_f) = 4.7D_{\text{ef}}^s$. The axial length of the surface is thus $L = 32D_{\text{ef}}^s$, which corresponds to a minimal Strouhal of St = 0.05. The cut off frequency based on the mesh size is about St = 6. The FWH formulation is applied with a closed surface. An open surface leads to an increase in the low-frequency acoustic level, as demonstrated by Shur et al. [44] and by Mendez et al. [56]. No correction is however applied to the FWH formulation in this study. Density fluctuations [44] induced by the hot primary stream and leaving the control volume are indeed weak, thanks to the mixing induced by the coaxial jets.

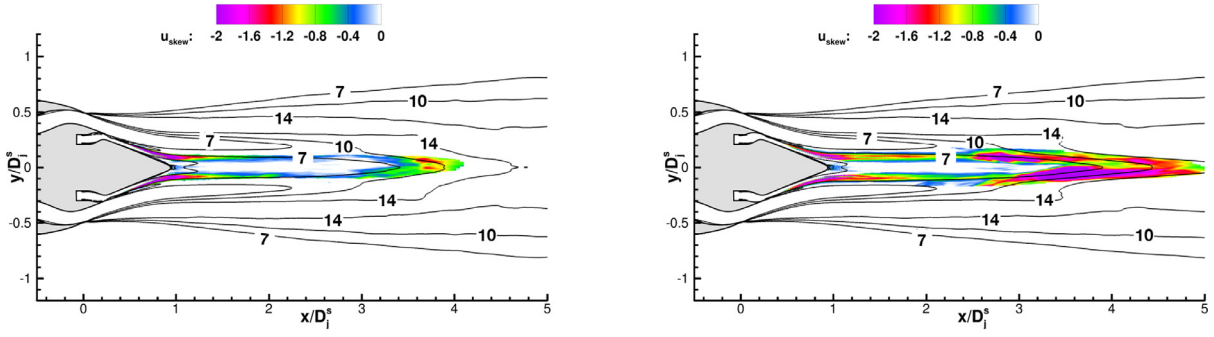

(a) T800 (b) T400

Fig. 16. Two dimensional mapping of the axial velocity skewness coefficient for (a) T800 et (b) T400. Iso-lines indicate level of the axial velocity standard deviation.

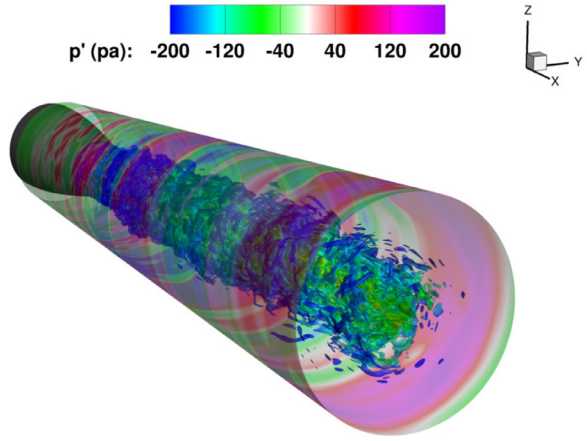

Fig. 17. Vorticity modulus isosurfaces colored by the axial velocity enclosed by the conical surface used for acoustic propagation via the Ffowcs-Williams et Hawkings (FWH) analogy, colored by pressure fluctuations.

Acoustic perturbations are propagated to the far-field and recorded by 2400 microphones positioned at $r = 6$m from $\theta = 20^\circ$ to 140°. For each polar angle position, 20 microphones are placed in the azimuthal direction in an uniform way. First, an acoustic validation is proposed based on the case T800 and then the temperature influence is analyzed. In the following, all acoustic results are normalized to a radial distance $r = 1$ m, from the primary nozzle exit plane $x = 0$, in assuming that acoustic sound pressure levels decrease as a function of $1/r$. In the following, all acoustic spectra are plotted as a function of the Strouhal number defined by $\mathrm{St} = f \times D^s_{ef}/U^s_j$.

5.1. T800 Configuration

Sound pressure level at $\theta = 30^\circ$ and 90° are plotted respectively in Fig. 18 (a) and (b). For an observer at 30°, the LES results are in agreement with the experimental data for $\mathrm{St} \geq 0.3$. However, in the vicinity of $\mathrm{St} = 0.2$ the noise level is under-estimated by about 7dB. This may be attributed to the lack of mesh discretization close to the secondary exhaust. Bogey [57] pointed out the importance of the mesh refinement in order to form, develop and transport large coherent structures. Theses structures play a key role in the flow development and in the sound generation specially at low frequencies. As a consequence, the underestimation of SPL at $\mathrm{St} = 0.2$ is here a signature of these structures in the region between the secondary jet exhaust and the jet core. For Strouhal number $\mathrm{St} > 2$, the noise level is slightly higher with a difference less than 1dB. At 90°, the noise emitted is highly related to the turbulence level close to the exit plane of the secondary stream. As seen in Section 4, a vortex pairing is present in the shear layer, which affects the noise generated perpendicular to the main flow direction. These observations have already been formulated by Bogey et al. [47]. For $\mathrm{St} > 1.5$, the LES predictions are 1 to 2 dB higher than the noise level from experimental measurements. The spectrum also shows some tonal components at $4 \leq \mathrm{St} \leq 6$. They have

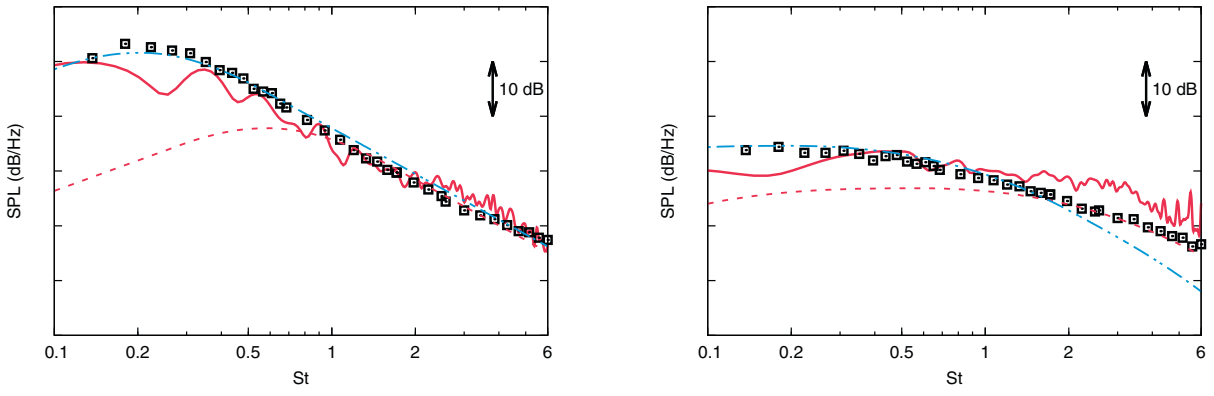

(a) (b)

Fig. 18. T800 case: acoustic spectra in far-field normalized to an observer distance of $r = 1m$ at θ : (a) 30° and (b) 90°. Two sources spectra from Tam [58] by using effective diameters and velocity exhaust of the primary and secondary streams : (a) Large scale similarity et (b) Fine scale similarity. —— LES and ⊡ Experiment. Tam spectra : — · — secondary stream ; — — — primary stream.

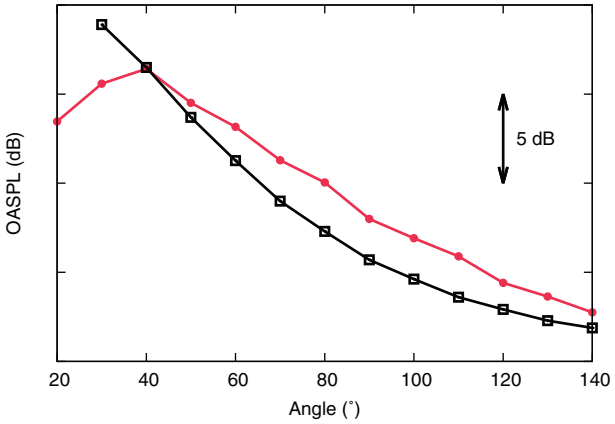

Fig. 19. T800 case: overall sound pressure level integrated on frequency between $0.2 \leq \mathrm{St} \leq 6$. —●— LES and —⊡— Experiment.

no physical meaning and are maybe caused by numerical spurious noise. However, for frequencies between $0.3 \leq \mathrm{St} \leq 1.5$, LES provides good acoustic results.

A simple identification of the acoustic contributions of each stream is proposed by the mean of Tam's empirical spectra [58]. Tam defined two kind of template, one for the acoustic radiation of coherent structures used at $\theta = 30^\circ$ and one for the acoustic radiation of fine scales used at $\theta = 90^\circ$. The spectral peak is first defined at $\mathrm{St} = 0.2$ for both kind of acoustic radiation. For the primary stream, the empirical law is calculated with the exit static temperature T_j^p and exit velocity U_j^p and the Strouhal is defined by $\mathrm{St}^p = f \times D_{ef}^p / U_j^p$. The same methodology is applied to determine the acoustic radiation of the secondary stream. The spectrum level are adapted individually according to the jet operating conditions and directivity angle [59]. At 30°, the noise radiated in the far-field is clearly dominated by the noise component from the large coherent structures of the secondary stream. At 90°, where acoustic perturbations are caused by fine scale structures of the flow, the noise from the secondary stream dominates the low-frequencies up to the crossing frequency $\mathrm{St} = 1.5$. The primary stream contribution represents the major part of the noise radiated for $\mathrm{St} \geq 1.5$.

In Fig. 19, the OASPL from LES and experimental data, obtained by integration of spectra between frequency range $0.2 \leq \mathrm{St} \leq 6$, are plotted for angles between 20° and 140°. For low angles $\theta < 40^\circ$, an underestimation of the noise level by approximately 2dB in the LES is observed. Against all expectations, for angles higher than 40°, the estimated noise level is slightly overestimated by less than 2dB. This additional noise is mostly due to high frequency spurious noise. The presence of the co-flow ($u/U_j^p = .05$) should indeed lead to a slight underestimation of the OASPL. Computation methodology applied for the T800 case gives good acoustic estimations. Moreover, this computation has been performed without the possibility to validate sensitive aerodynamic values for noise generation, like shear layer thickness and the level of turbulence intensity due to the lack of exploitable experimental data.

As already mentioned before, the grid resolution in the azimuthal direction is the limiting parameter of the present simulation. For realistic geometries, the strategy based on a structured

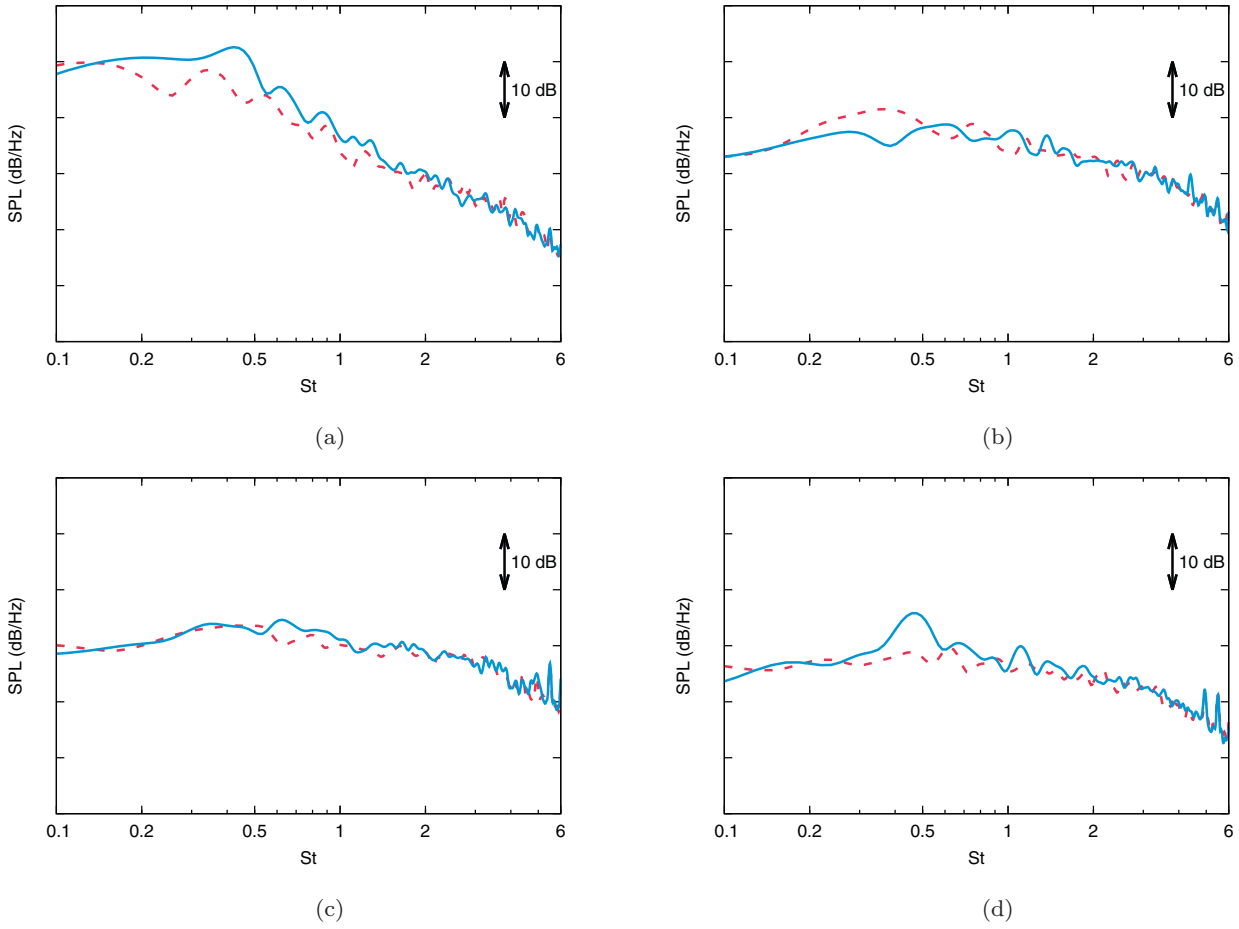

Fig. 20. Acoustic spectra in far-field normalized to an observer distance of $r = 1m$ for θ : (a) 30°, (b) 60°, (c) 90° and (d) 130°. – – – T800 and —— T400.

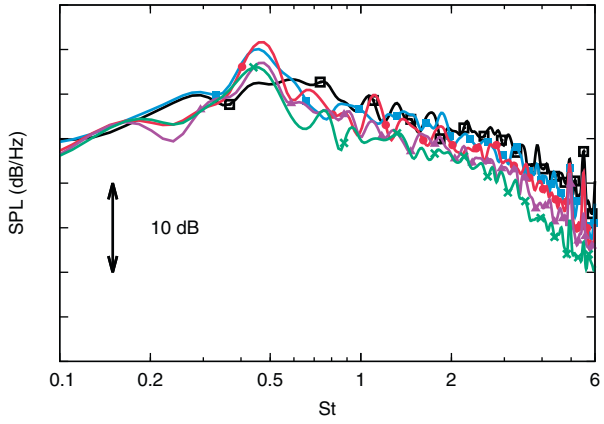

Fig. 21. Acoustic spectra in far-field related to $r = 1m$ for the case T400 for an angle θ between 110° and 150°. —□— : $\theta = 110°$; —■— : $\theta = 120°$; —●— : $\theta = 130°$; —▲— : $\theta = 140°$; —×— : $\theta = 150°$.

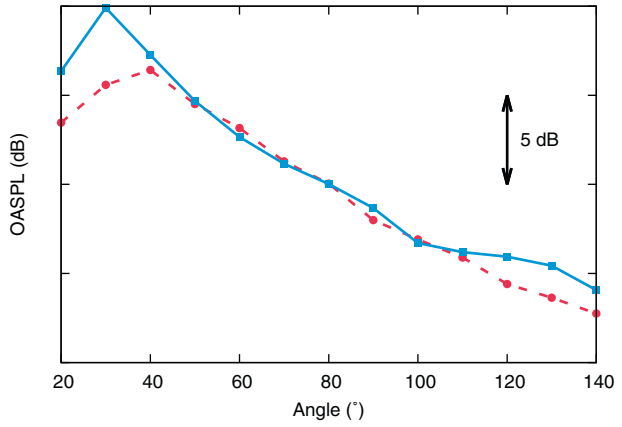

Fig. 22. OASPL integrated over $0.2 \leq St \leq 6$ for cases T800 and T400. —●— T800 and —■— T400.

meshing approach is probably reached here, at least for the present solver.

5.2. Temperature effects on far-field noise

Comparisons between the T800 and T400 jets are shown in Fig. 20 for polar angles 30°, 60°, 90° and 130°. For $\theta = 30°$ (Fig. 20 (a)), the low frequency noise level $St \leq 1.5$ is higher for the T400 jet. This result is in agreement with the velocity skewness fields (Fig. 16), an indicator of turbulence intermittency. For higher frequencies $St > 1.5$, the modification of the primary stream temperature has no impact on the acoustic radiation, in contrast to what is observed for a single jet [60]. At 60° (Fig. 20 (b)), noise level is 4dB higher close to $St = 0.35$ for the T800 case whereas for higher frequencies, no difference can be observed between the two configurations. For an angle of 90° (Fig. 20 (c)), there is no difference for all the frequency range. At this angle, the major part of the acoustic radiation is due to the secondary stream. However, an extra bump about 8dB is clearly visible at 130° and $St = 0.46$ for T400 case (Fig. 20 (d)) and will be discussed in the next section. The acoustic radiation of this unknown component starts to be visible for an angle close to 120° until 150° with a maximum for $\theta = 130°$ as plotted in Fig. 21.

The OASPL integrated for frequency between $0.2 \leq St \leq 6$ are plotted in Fig. 22 for the two jets. For angles between 50° and 110°, the acoustic noise level is not influenced by the temperature of the primary stream with less than 1 dB difference. However, for angles outside of these bounds, the jet T400 is louder than the jet T800 with a difference up to 4 dB. Indeed, in a dual-streams configuration, temperature effect in the primary stream has a limited influence on noise generation compared to a single stream configuration. As shown in Fig. 18 (a) and (b), most of the acoustic radiation is caused by the secondary stream, which has a mass flow rate 10 times higher than the primary stream. Higher acoustic levels for small angles is linked to the higher intermittent behaviour of the case T400 but nothing can explain the difference for the upstream acoustic radiation ($\theta > 110°$). The last part of this work is devoted to finding the physical mechanism of this acoustic radiation.

6. Acoustic trapped waves in the jet core

6.1. Description of the phenomenon

Some recent works [28,29] have shown that a subsonic single jet could produce tonal noise in the near field for axial positions corresponding to the nozzle exit plane. Moreover, these tones are sensitive to jet exhaust conditions. Towne et al. [25] have demonstrated that tonal components are produced by acoustic trapped waves in the potential core. Their study is based on the numerical database of Brés et al. [61], which is a single stream isothermal jet at $M_j = 0.9$.

A way to reveal the presence of this kind of waves in the potential core is to perform a frequency-wavenumber decomposition of the pressure signal on the jet centerline. A regular line array (226 probes) is thus considered on the jet axis with axial spacing increments of $\Delta x = 0.045 D_j^s$ between $x = 0.94 D_j^s$ and $x = 11.12 D_j^s$. The diagrams obtained with this procedure are displayed in Fig. 23 (a) for T800 and (b) for T400. Three lines are also plotted (Fig. 23 (b)), representing the wave celerity in agreement with the dispersion relation $k = \omega/c$, where ω is the frequency, k is the wave number and c the wave celerity. Three celerities are chosen, one is the convection velocity $u_c = 0.7 U_j^p$ (solid line), second the free upstream acoustic wave $-c_0$ (dashed-dotted line) and then the upstream acoustic wave slowed down by the jet flow $u_c - c_0$ (dashed line).

Moreover, the cylindrical soft duct model proposed by Towne et al. [25] is also plotted on the diagram (dotted line). This model provides the dispersion relation between wave number modes and frequencies for an azimuthal mode m as

$$k_d^{\pm} = \frac{-\omega M \pm \sqrt{T_r}\sqrt{\omega^2 - 4(T_r - M^2)\beta_m^2}}{T_r - M^2} \tag{2}$$

where $\omega = 2\pi St M$ is the normalized frequency, $T_r = T_j/T_0$ is the temperature ratio, M is the acoustic Mach number with $M_j = M/\sqrt{T_r}$, and $\beta_m = i\gamma_i/2$ is the first root of the Bessel function J_m, with $\gamma_i = \sqrt{k^2 - (\omega - Mk)^2/T}$. For the first azimuthal mode of the T400 case, the values are $T_r = 1.4$, $M = 1$ and $\beta_0 = 2.4048$. Only the first azimuthal mode is here considered. In the two jets, the most energetic band corresponds to the well known Kelvin-Helmholtz instability waves (Fig. 23) and the group velocity is close to $0.7 U_j^p$. For the jet T800, upstream waves are not detected, whereas for the T400 case a band of energy with a negative phase velocity is observed. The group velocity is bounded by $-c_0$ and $u_c - c_0$. For this wave packet, the energy is concentrated around the Strouhal value of $St = 0.46$. Two important observations can thus be made: first, the single round jet vortex sheet model given by Towne et al. [25] provides a good estimation of the frequency modes of the trapped waves in a complex dual-stream configuration. Secondly, trapped waves phenomenon can occur in non-potential jet flows.

Towne et al. [25] have also explored the sensitivity for the presence of trapped waves to the operating conditions. In their work, a necessary condition to find trapped waves is to detect two saddle

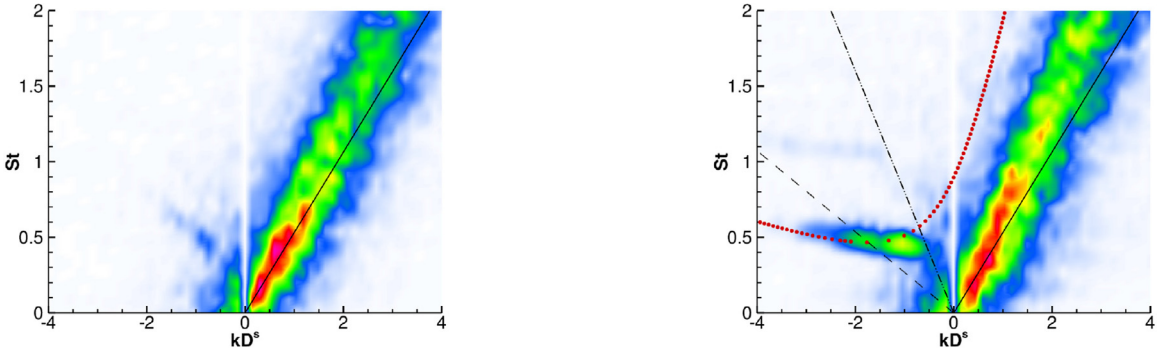

Fig. 23. Frequency-wavenumber diagram from probes on jet axis: (a) T800 and (b) T400. The lines represent waves with constant group and phase velocity with dispersion relation $k = \omega/c$, where c is the wave celerity, ω is the frequency and k is the wave number: —— $u_c = 0.7U_j^p$; —·— $-c_0$; – – – $u_c - c_0$ and ● cylindrical soft duct model from Towne et al. [25].

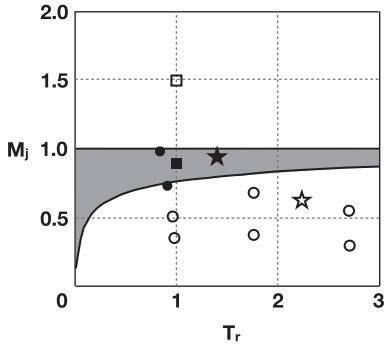

Fig. 24. Diagram $(M_j, T_r = T_j/T_0)$. Gray area represents exhaust conditions where acoustic resonance can occur according to Towne et al. [25]. Closed symbols are jets where trapped waves have been observed. Open symbols are jets where trapped waves have not been observed. ■ numerical jets ; • experimental jets; ☆ T800 et ⋆ T400.

points by the vortex sheet model for a given couple $(M_j, T_r = T_j/T_0)$. Fig. 24 summarizes this condition for the first azimuthal and radial mode. The grey area corresponds to the couple of (M_j, T_r) where trapped waves could be observed. This area is delimited by $M_j = 1$ for which the saddle point asymptotically vanishes. Single jets with different operating conditions provided by Towne et al. [25] are also added to this diagram. As expected, if the primary stream operating conditions are considered, the jet T800 is out of the gray area whereas the case T400 is in. This diagram confirms the previous observations. In a dual-stream jet, the couple $(M_j, T_r = T_j^p/T_0)$ of the primary stream has to be considered to determine the presence of trapped waves in the jet core.

In order to determine the axial position of the generation of trapped waves inside the dual-stream jet core, snapshots of the filtered fluctuating pressure field at St = 0.46 over one period T are plotted in Fig. 25 (a) to (h). To filter the fluctuating pressure, a two-dimensional discrete Fourier transform is performed to obtain the pressure field in the frequency domain. The number of snapshots allow a frequency resolution of St = 0.03 between two modes. The mode at St = 0.46 is then extracted and transformed back in the temporal domain using an inverse transform. Two waves called k^- and k^+ are identified by an arrow on each snapshot. Initially, the wave k^- is defined at $x = 1.6D_j^s$ and the wave k^+ at $x = 2.2D_j^s$ in Fig. 25 (a). Following the time advancement, from $t = 0$ up to $t = 7T/8$, the wave k^- clearly travels upstream with an amplitude modulation, whereas the wave k^+ is going downstream. Two waves k^+ and k^- are clearly produced in the vicinity of $x = 2D_j^s$. This occurs before the end of the length core jet as observed by Towne et al. [25], and is called the wave turning point. The spatio-temporal correlation of the filtered pressure signal on the jet axis is plotted in Fig. 26 (a) for an axial position $x = 1.3D_j^s$ and (b) for $x = 3.0D_j^s$, respectively upstream and downstream the wave turning point. These correlation maps enabled a more quantitative identification of the production area of the waves k^- and k^+. For the wave k^-, the correlation path is high for $1 \leq x/D_j^s \leq 1.8$ (Fig. 26 (a)). As expected, the convection velocity is negative and its amplitude is lower than the downstream wave about $c_{k^-} = u_c - c_j$ where u_c is the convection velocity. For the wave k^+ in Fig. 26 (a), the correlation coefficient is close to 1 between $x = 1.8D_j^s$ up to $x = 3.8D_j^s$. On the contrary, its convection velocity is positive. As a conclusion from these two maps, the trapped wave turning point emerges near $x = 1.8D_j^s$.

6.2. Impact on noise

As seen in Fig. 20 (d), the trapped wave has a strong influence on jet noise radiated in the far-field whereas Towne et al. [25] have detected these tones only in the near-field of a single stream jet. The fact that this phenomenon propagates in the far-field can be explained principally by the presence of the central plug in the geometry. In order to characterize the modal structure of the radiated noise, an azimuthal decomposition of the acoustic near-field of the T400 case is shown in Fig. 27 for the modes $m = 0$ (a) and $m = 1$ (b). Only the two first modes are shown, because they contain more than 90% of the total acoustic energy. The azimuthal decomposition is based on a azimuthal array of 20 microphones defined in the physical domain at $r = 2.5D_s^j$ for $-1 \leq x/D_j^s \leq 16$ with an axial spacing increment $\Delta x = 0.045D_j^s$.

For the mode $m = 0$, a peak is clearly visible for $x/D_j^s \leq 0$ at St = 0.46. Nevertheless, the noise level is lower than those observed downstream the jet core ($x/D_j^s \geq 10$). On the contrary, no conclusion can be made regarding the mode $m = 1$ (Fig. 27 (b)), as no energy peak appears on the SPL map. For downstream positions, the noise level is related to the flow behavior rather than acoustic resonance in the core jet. To confirm this hypothesis, the filtered acoustic and aerodynamic pressure field at frequency St = 0.46 shown in Fig. 28 is analyzed.

The aerodynamic pressure is plotted from -1000 to 1000 Pa and the acoustic one from -20 to 20 Pa to handle with the large dynamic range. Acoustic waves propagating in all directions are clearly visible. In order to characterize the origin of these waves, the coherence function C_{pp} between a probe close to the plug and two microphones at $r = 2.5D_j^s$, one upstream at $x/D_j^s = -0.5$ and

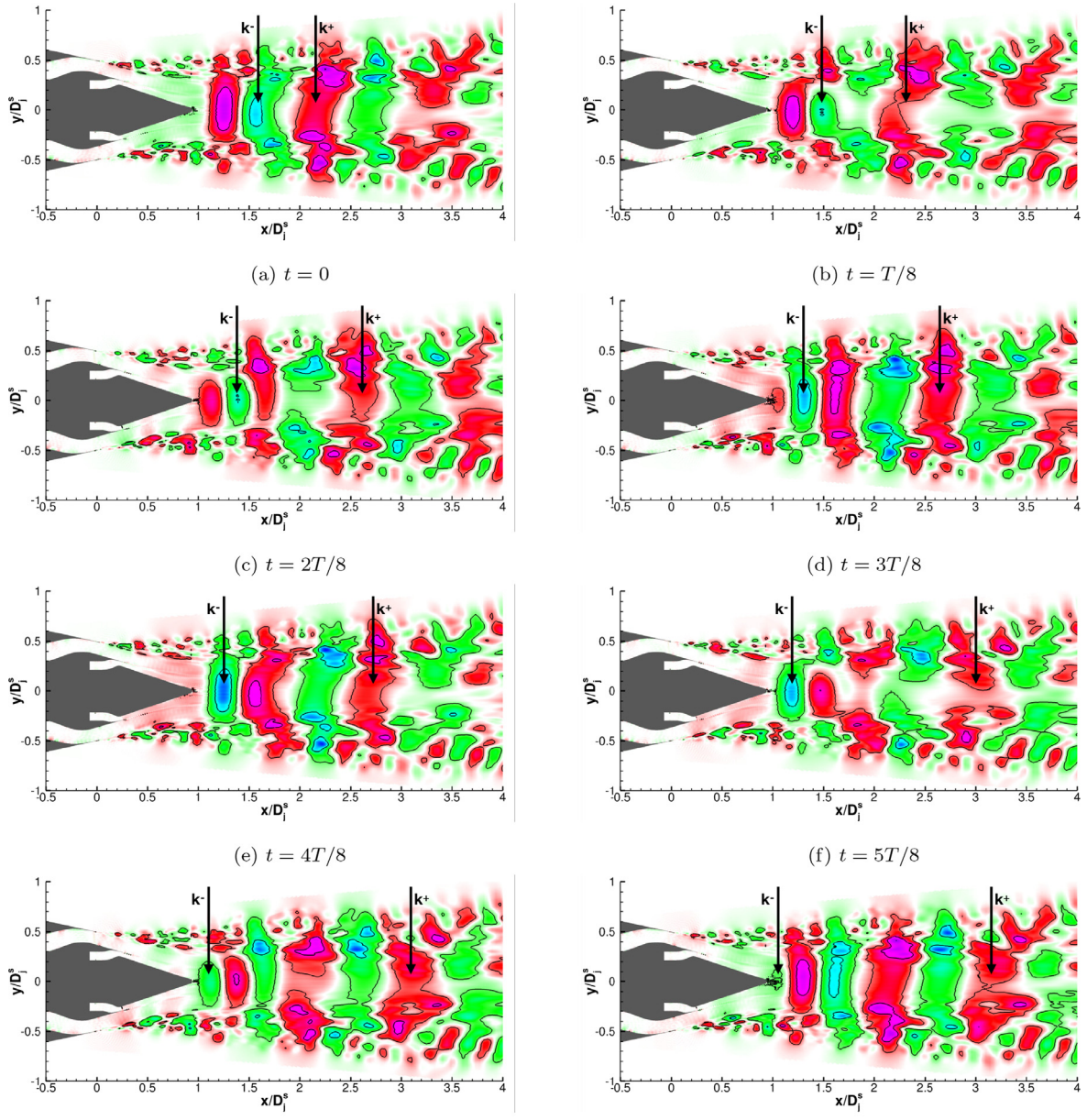

(a) $t = 0$ (b) $t = T/8$ (c) $t = 2T/8$ (d) $t = 3T/8$ (e) $t = 4T/8$ (f) $t = 5T/8$ (g) $t = 6T/8$ (h) $t = 7T/8$

Fig. 25. T400 case: Instantaneous snapshots of the filtered pressure at St = 0.46 over a period T.

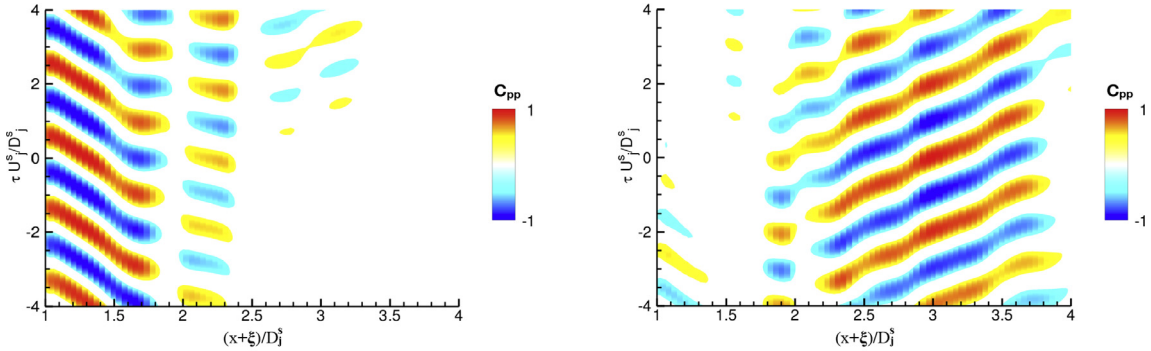

(a) (b)

Fig. 26. T400 case: Spatio-temporal correlation maps from the filtered pressure at St = 0.46 on the jet axis for an initial position : (a) $x = 1.3D_j^s$ and (b) $x = 3.0D_j^s$.

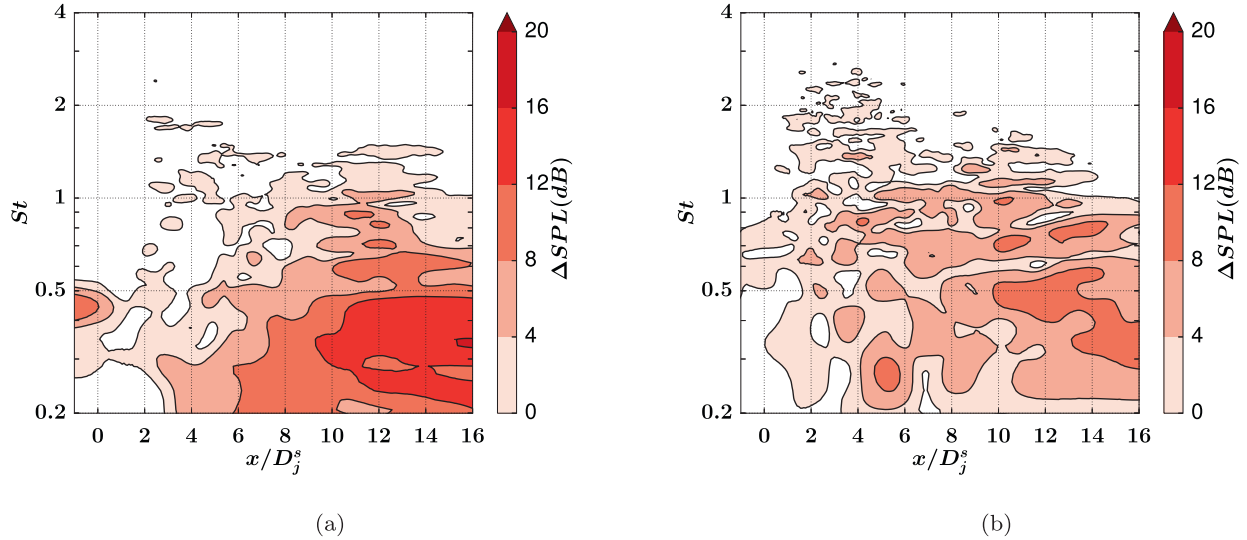

Fig. 27. T400 case: SPL for a microphone located at $r = 2.5D_s^j$ (a) azimuthal mode 0 and (b) azimuthal mode 1.

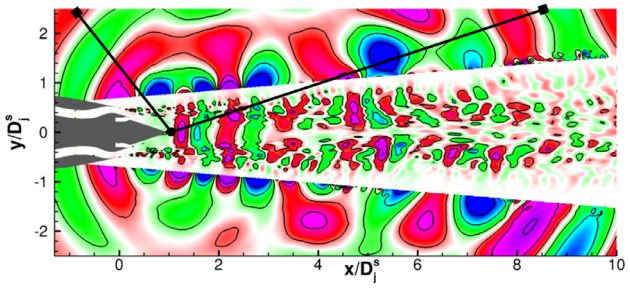

Fig. 28. T400 case: Instantaneous snapshots of the filtered pressure at St = 0.46. Dynamic range inside the flow comes from −1000 to 1000*Pa* and from −20 to 20*Pa* outside the flow. The two microphones chosen for the coherence function are indicated by squares and the probe inside the jet core by the point at the plug tip.

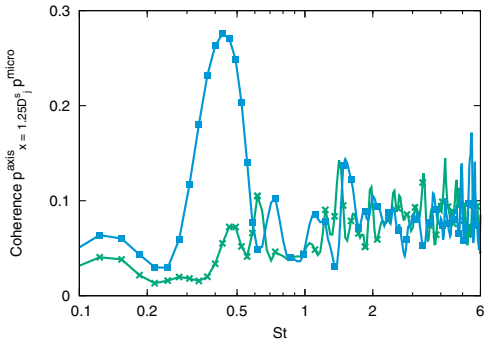

Fig. 29. T400 case: Coherence function (C_{pp}) between pressure for probes at $x = 1.25D_j^s$ and acoustic pressure at two positions : —■— $r = 2.5D_j^s$ et $x = -0.9D_j^s$ ($\theta = 130°$) ; —×— $r = 2.5D_j^s$ and $x = 9D_j^s$ ($\theta = 30°$).

another one downstream at $x/D_j^s = 9$, are plotted in Fig. 29. The probe and two microphones are respectively indicated by the circle and the two square in Fig. 28.

For the upstream microphone, the coherence function shows a peak at St = 0.46 with $C_{pp} = 0.28$. The upstream acoustic radiation is thus correlated with the acoustic wave trapped in the core jet. On the other hand, for the downstream microphone, the coherence function does not display a clear peak for any frequencies. This result indicates that no link can be established between the acoustics radiated for aft angles and the events that occur in the vicinity of the plug tip. On the contrary, the acoustic wave and the noise peak observed in the near- and far-field for high angles are clearly related to the interaction of the trapped wave k^- with the central plug.

7. Conclusion

The influence of temperature effects on complex dual-stream jets including a central plug has been carried out in this study. The results have been obtained by high-fidelity LES, based on sixth-order numerical schemes. The algorithm is combined with an explicit filtering to drain the energy cascade at the cut-off wavenumber while leaving the resolved scales unaffected by this filtering.

Numerical results have been generally found in agreement with the corresponding experiments of the EXEJET program. The primary stream temperature is observed to have a small influence on the aerodynamic development of the dual-stream jet from the nozzle. In fact, no significant influence of the well-known bi-polar source induced by the temperature fluctuations occurs in a realistic configuration. Indeed, the aerodynamic jet behavior is mostly driven by the secondary stream in a high by-pass-ratio nozzle. As a consequence, the convection velocity is not significantly affected with the temperature increase. On the contrary, the jet core length is reduced when the primary stream is heated, as for a single jet, in agreement with changes also observed on the axial velocity fluctuations.

An additional acoustic source is also found in the cold case for upstream angles at St = 0.46. This study highlights the existence of trapped wave in non-potential jet flow. It is shown that this acoustic source is caused by trapped waves in the jet core interacting with the central plug. Moreover, a good estimation of the frequency modes of these waves is provided by a vortex sheet model developed for single jets [25]. Finally, in a complex dual-stream configuration, the couple (M_j, T_j) of the primary stream has to be considered to determine the presence of trapped waves in the jet core. The consideration of an installed configuration with a dual stream jet in the vicinity of a wing could amplified this phenomena.

Declaration of Competing Interest

The authors declare that they have no known competing financial interests or personal relationships that could have appeared to influence the work reported in this paper.

CRediT authorship contribution statement

Romain Biolchini: Writing - original draft, Writing - review & editing, Investigation, Formal analysis, Conceptualization, Methodology, Software, Visualization. **Guillaume Daviller:** Writing - original draft, Writing - review & editing, Investigation, Formal analysis, Visualization, Supervision. **Christophe Bailly:** Writing - original draft, Writing - review & editing, Investigation, Formal analysis, Supervision. **Guillaume Bodard:** Writing - review & editing, Resources.

Acknowledgements

This work was granted access to the HPC resources of CINES under the allocation 2017-[x20172a6074] made by GENCI. The authors acknowledge the support of Airbus Operation SAS, Safran Aircraft Engines and Onera partners for the provision of the EXEJET database.

References

[1] Bogey C, Bailly C, Juvé D. Noise investigation of a high subsonic, moderate reynolds number jet using a compressible large eddy simulation. Theor Comput Fluid Dyn 2003;16(4):273–97. doi:10.1007/s00162-002-0079-4.
[2] Shur ML, Spalart PR, Strelets MK, Travin AK. Towards the prediction of noise from jet engines. Int J Heat Fluid Flow 2003;24(4):551–61. doi:10.1016/S0142-727X(03)00049-3.
[3] Andersson N, Eriksson L-E, Davidson L. Large-eddy simulation of subsonic turbulent jets and their radiated sound. AIAA J 2005;43(9):1899–912. doi:10.2514/1.13278.
[4] Bodony D, Lele SK. Current status of jet noise predictions using large-Eddy simulation. AIAA J 2008;46(2):364–80. doi:10.2514/1.24475.
[5] Bogey C, Marsden O. Simulations of initially highly disturbed jets with experiment-Like exit boundary layers. AIAA J 2016;54(4):1299–312. doi:10.2514/1.J054426.
[6] Bogey C, Barré S, Juvé D, Bailly C. Simulation of a hot coaxial jet: direct noise prediction and flow-acoustics correlations. Phys Fluids 2009;21(3):1–14. doi:10.1063/1.3081561.
[7] Viswanathan K, Shur M, Spalart P, Strelets M. Flow and noise predictions for single and dual-Stream beveled nozzles. AIAA J 2008;46(3):601–26. doi:10.2514/1.27299.
[8] Andersson N, Eriksson L-E, Davidson L. LES prediction of flow and acoustic field of a coaxial jet. In: 11th AIAA/CEAS Aeroacoustics Conference, no. AIAA 2005–2884; 2005. p. 1–26. doi:10.2514/6.2005-2884.
[9] Eastwood S, Xia H, Tucker P. Large-eddy simulation of complex geometry jets. J Propul Power 2012;28(2):235–45. doi:10.2514/1.B34322.
[10] Mockett C, Haase W, Schwamborn D. Go4Hybrid: grey area mitigation for hybrid RANS-LES methods: results of the 7th framework research project go4hybrid, funded by the european union, 2013–2015, 134. Springer; 2017. doi:10.1007/978-3-319-52995-0.
[11] Le Bras S, Deniau H, Bogey C, Daviller G. Development of compressible large-Eddy simulations combining high-Order schemes and wall modeling. AIAA J 2017;55(4):1–12. doi:10.2514/1.J055107.
[12] Brès GA, Ham FE, Nichols JW, Lele SK. Unstructured large-eddy simulations of supersonic jets. AIAA J 2017;55(4):551–61. doi:10.2514/1.J055084.
[13] Murakami E, Papamoschou D. Mean flow development in dual-stream compressible jets. AIAA J 2002;40(6):1131–8. doi:10.2514/2.1762.
[14] Tinney C, Jordan P. The near pressure field of co-axial subsonic jets. J Fluid Mech 2008;611(1):175–204. doi:10.1017/S0022112008001833.
[15] Huber J, Drochon G, Bonnaud C, Pintado-Peno A, Cléro F, Bodard G. Large-scale jet noise testing, reduction and methods validation "EXEJET": 1. Project overview and focus on installation. In: 20th AIAA/CEAS aeroacoustics conference, no. AIAA 2014–3032; 2014. p. 1–17. doi:10.2514/6.2014-3032.
[16] David F, Jourdan JM, Cléro F, Koenig M, Huber J. Large-scale jet noise testing, reduction and methods validation "EXEJET": 4 - Flows characterization with PIV in the CEPRA19 anechoic wind tunnel of Onera. In: 20th AIAA/CEAS Aeroacoustics Conference, no. AIAA 2014–3035; 2014. p. 1–11. doi:10.2514/6.2014-3035.
[17] Fisher M, Lush P, Harper Bourne M. Jet noise. J Sound Vib 1973;28(3):563–85. doi:10.1016/S0022-460X(73)80040-9.
[18] Tanna H. An experimental study of jet noise part i: turbulent mixing noise. J Sound Vib 1977;50(3):405–28. doi:10.1016/0022-460X(77)90493-X.
[19] Lilley G. The radiated noise from isotropic turbulence with applications to the theory of jet noise. J Sound Vib 1996;190(3):463–76. doi:10.1006/jsvi.1996.0074.
[20] Viswanathan K. Aeroacoustics of hot jets. J Fluid Mech 2004;51(1):39–82. doi:10.1017/S0022112004000151.
[21] Bridges J, Wernet M. Establishing Consensus Turbulence Statistics for Hot Subsonic Jets. In: 16th AIAA/CEAS Aeroacoustics Conference, no. AIAA 2010–3751; 2010. p. 1–41. doi:10.2514/6.2010-3751.
[22] Zaman KBMQ. Far-field noise of a subsonic jet under controlled excitation. J Fluid Mech 1985;152:83–111. doi:10.1017/S0022112085000581.
[23] Bogey C, Bailly C. Large eddy simulations of transitional round jets: influence of the reynolds number on flow development and energy dissipation. Phys Fluid 2006;18(6):1–15. doi:10.1063/1.2204060.
[24] Bogey C, Marsden O. Numerical investigation of temperature effects on properties of subsonic turbulent jets. In: 19th AIAA/CEAS Aeroacoustics Conference, no. AIAA 2013–2140; 2013. p. 1–19. doi:10.2514/6.2013-2140.
[25] Towne A, Cavalieri A, Jordan P, Colonius T, Schmidt O, Jaunet V, et al. Acoustic resonance in the potential core of subsonic jets. J Fluid Mech 2017;825(1):1113–52. doi:10.1017/jfm.2017.346.
[26] Fisher MJ, Preston GA, Mead CJ. A modelling of the noise from simple coaxial jets, part II: with heated primary flow. J Sound Vib 1998;209(3):405–17. doi:10.1006/jsvi.1997.1217.
[27] Viswanathan K. Parametric study of noise from dual-stream nozzles. J Fluid Mech 2004;521(1):35–68. doi:10.1017/S0022112004000813.
[28] Suzuki T, Colonius T. Instability waves in a subsonic round jet detected using a near-field phased microphone array. J Fluid Mech 2006;565(1):197–226. doi:10.1017/S0022112006001613.
[29] Sinha A. Development of reduced-order models and strategies for feedback control of high-speed axisymmetric jets. The Ohio State University; 2011. Ph.D. thesis.
[30] Cambier L, Heib S, Plot S. The onera elsa CFD software: input from research and feedback from industry. Mech Ind 2013;14(3):159–74. doi:10.1051/meca/2013056.
[31] Bogey C, Bailly C. A family of low dispersive and low dissipative explicit schemes for flow and noise computations. J Comput Phys 2004;194(1):194–214. doi:10.1016/j.jcp.2003.09.003.
[32] Fosso Pouangue A, Deniau H, Sicot F, Sagaut P. Curvilinear finite-volume schemes using high-order compact interpolation. J Comput Phys 2010;229(13):5090–122. doi:10.1016/j.jcp.2010.03.027.
[33] Visbal M, Gaitonde D. Very high-Order spatially implicit schemes for computational acoustics on curvilinear meshes. J Comput Acoust 2001;9(4):1259–86. doi:10.1142/S0218396X01000541.
[34] Bogey C, Bailly C. Decrease of the effective reynolds number with eddy-Viscosity subgrid modeling. AIAA J 2005;43(2):437–9. doi:10.2514/1.10665.
[35] Bogey C, Bailly C. Three-dimensional non-reflective boundary conditions for acoustics simulations: far field formulation and validation test cases. Acta Acustica united Acustica 2002;88(1):463–71.
[36] Tam C, Dong Z. Radiation and outflow boundary conditions for direct computation of acoustics and flow disturbances in a nonuniform mean flow. J Comput Acoust 1996;4(2):175–201. doi:10.1142/S0218396X96000040.
[37] Bodony D. Analysis of sponge zones for computational fluid mechanics. J Comput Phys 2006;212(2):681–702. doi:10.1016/j.jcp.2005.07.014.
[38] Fosso Pouangue A, Deniau H, Lamarque N, Poinsot T. Comparison of outflow boundary conditions for subsonic aeroacoustic simulations. Int J Numer Methods Fluids 2012;68(10):1207–33. doi:10.1002/fld.2597.
[39] Tam C, Webb J. Dispersion-Relation-Preserving finite difference schemes for computational acoustics. J Comput Phys 1993;107(2):262–81. doi:10.1006/jcph.1993.1142.
[40] Fosso Pouangue A, Deniau H, Lamarque N. A sixth-order compact finite-volume scheme for aeroacoustics: application to a large eddy simulation of a jet. In: V European Conference on Computational Fluid Dynamics; 2010. p. 1–15.
[41] Bogey C, Bailly C. Effects of inflow conditions and forcing on subsonic jet flows and noise. AIAA J 2005;43(5):1000–7. doi:10.2514/1.7465.
[42] Reichardt H. The principles of turbulent heat transfer. Tech. Rep.; 1957.
[43] Shur M, Spalart P, Strelets M. Noise prediction for increasingly complex jets. part II: applications. Int J Aeroacoust 2005;4(3):247–66. doi:10.1260/1475472054771385.
[44] Shur M, Spalart P, Strelets M. Noise prediction for increasingly complex jets. part i: methods and tests. Int J Aeroacoust 2005;4(3):213–45. doi:10.1260/1475472054771376.
[45] Shur M, Spalart P, Strelets M, Garbaruk A. Further steps in LES-based noise prediction for complex jets. In: 44th AIAA Aerospace Sciences Meeting and Exhibit, no. AIAA 2006-485; 2006. p. 1–26. doi:10.2514/6.2006-485.
[46] Spalart P, Allmaras S. A one-equation turbulence model for aerodynamic flows. La Recherche Aerospatiale 1994;1(1):5–21. doi:10.2514/6.1992-439.
[47] Bogey C, Marsden O, Bailly C. Large-eddy simulation of the flow and acoustic fields of a reynolds number 10e5 subsonic jet with tripped exit boundary layers. Phys Fluids 2011;23(3):1–20. doi:10.1063/1.3555634.
[48] Bodony D, Lele SK. Jet noise prediction of cold and hot subsonic jets using large-eddy simulation. In: 10th AIAA/CEAS Aeroacoustics Conference, no. AIAA 2004–3022; 2004. p. 1–17. doi:10.2514/6.2004-3022.
[49] Doty HBS, Michael J, Kinzie KW. Turbulence measurements of separate-flow nozzles with pylon interaction using particle image velocimetry. AIAA J 2017;45(6):1281–9. doi:10.2514/1.20420.
[50] Brès G, Ham FE, Nichols JW, Lele SK. Nozzle wall modeling in unstructured large eddy simulations for hot supersonic jet predictions. In: 19th AIAA/CEAS aeroacoustics Conf., no. AIAA 2013–2142; 2013. p. 1–19. doi:10.2514/6.2013-2142.
[51] Bogey C. A study of the effects of temperature on velocity and density fluctuations in high-subsonic jets. In: 52nd Aerospace sciences meeting, no. AIAA 2014-0524; 2014. p. 1–15. doi:10.2514/6.2014-0524.
[52] Panda J. Experimental investigation of turbulent density fluctuations and noise generation from heated jets. J Fluid Mech 2007;591(1):73–96. doi:10.1017/S0022112007007173.

[53] Bridges J. Effect of heat on space-time correlations in jets. In: 12th AIAA/CEAS aeroacoustics conference, no. AIAA 2006–2534; 2006. p. 1–16. doi:10.2514/6.2006-2534.
[54] Lau J. Effects of exit mach number and temperature on mean-flow and turbulence characteristics in round jets. J Fluid Mech 1981;105(1):193–218. doi:10.1017/S0022112081003170.
[55] Casalino D. An advanced time approach for acoustic analogy predictions. J Sound Vib 2003;261(4):583–612. doi:10.1016/S0022-460X(02)00986-0.
[56] Mendez S, Shoeybi M, Lele SK, Moin P. On the use of the Ffowcs Williams-Hawkings equation to predict far-field jet noise from large-eddy simulations. Int J Aeroacoust 2013;12(1–2):1–20. doi:10.1260/1475-472X.12.1-2.1.
[57] Bogey C. Grid sensitivity of flow field and noise of high-Reynolds-number jets computed by large-eddy simulation. Int J Aeroacoust 2018;17(4–5):399–424. doi:10.1177/1475472X18778287.
[58] Tam C, Golebiowski M, Seiner J. On the two components of turbulent mixing noise from supersonic jets. In: 2nd AIAA/CEAS aeroacoustics conference, no. AIAA 96–1716; 1996. p. 1–17. doi:10.2514/6.1996-1716.
[59] Viswanathan K. Analysis of the two similarity components of turbulent mixing noise. AIAA J 2002;40(9):1735–44. doi:10.2514/2.1878.
[60] Biolchini R, Bailly C, Boussuge J-F, Fernando R. Numerical study on the relation between hydrodynamic fluctuations and noise in hot jets at high Reynolds number. In: 22nd AIAA/CEAS aeroacoustics conference, no. AIAA 2016–3048; 2016. p. 1–15. doi:10.2514/6.2016-3048.
[61] Brès G, Jordan P, Colonius T, Le Rallic M, Jaunet V, Lele SK. Large eddy simulation of a mach 0.9 turbulent jet. Center Turbul Res Proc Summer Program 2014 2014;1(1):221–30.